JEM Journal of Experimental Medicine

BRIEF DEFINITIVE REPORT

Corticospinal circuit remodeling after central nervous system injury is dependent on neuronal activity

Peter M. Bradley[1,2]*, Carmen K. Denecke[1,2,4]*, Almir Aljovic[1,2,4], Anja Schmalz[1,2], Martin Kerschensteiner[1,2,3], and Florence M. Bareyre[1,2,3]

The remodeling of supraspinal axonal circuits mediates functional recovery after spinal cord injury. This process critically depends on the selection of appropriate synaptic connections between cortical projection and spinal relay neurons. To unravel the principles that guide this target selection, we used genetic and chemogenetic tools to modulate NMDA receptor (NMDAR) integrity and function, CREB-mediated transcription, and neuronal firing of relay neurons during injury-induced corticospinal remodeling. We show that NMDAR signaling and CREB-mediated transcription maintain nascent corticospinal tract (CST)–relay neuron contacts. These activity-dependent signals act during a defined period of circuit remodeling and do not affect mature or uninjured circuits. Furthermore, chemogenetic modulation of relay neuron activity reveals that the regrowing CST axons select their postsynaptic partners in a competitive manner and that preventing such activity-dependent shaping of corticospinal circuits limits motor recovery after spinal cord injury.

Introduction

The remodeling of neuronal circuits is the structural basis for functional recovery of the damaged central nervous system (CNS; Bareyre et al., 2004; Kerschensteiner et al., 2004; Courtine et al., 2008; Ueno et al., 2012; Zörner et al., 2014). For example, after an incomplete spinal cord injury (SCI), the transected hindlimb corticospinal tract (CST) spontaneously forms an intraspinal "detour circuit" that reestablishes a functional connection between CST projection neurons and their lumbar projection area. For this detour circuit to form, CST projection neurons first extend new collaterals into the cervical gray matter, where they make new synaptic contacts with different populations of intraspinal relay neurons (Fig. 1 A). These contacts are subsequently refined and preferentially maintained on neurons, such as long propriospinal neurons (LPSN), that provide relay connections to the original CST target area (Bareyre et al., 2004). Appropriate target selection of CST collaterals during both the initial phase of contact formation and the later pruning phase is required to allow selective compensation of disturbed neuronal pathways without inducing maladaptive responses. It is thus critical for endogenous functional restoration (Bareyre et al., 2004; Courtine et al., 2008; Hollis et al., 2015; Jacobi et al., 2015) as well as for enhanced recovery following neurostimulation and neurorehabilitation (van den Brand et al., 2012; Hilton et al., 2016). Yet how regrowing collaterals in the injured CNS decide which synapses to maintain or remove is not well understood.

Neurons in the developing nervous system face a similar challenge. Indeed, a hallmark of developmental circuit formation is that postsynaptic cells are initially contacted by many presynaptic partners before synaptic elimination processes remove excessive connections and establish mature connectivity (Katz and Shatz, 1996; Sanes and Lichtman, 1999; Okawa et al., 2014). Several lines of evidence indicate that activity-dependent signals play a key role during the developmental refinement of such connections. For example, it has been demonstrated that an imbalance in neurotransmission promotes selective connectivity (Buffelli et al., 2003), and that perturbing excitatory neurotransmission via inhibition of N-methyl-D-aspartate receptors (NMDARs; Iwasato et al., 2000; Arakawa et al., 2014) or their downstream signals (Flavell and Greenberg, 2008) disrupts circuit refinement. Here we modulated neuronal firing and activity-dependent signaling of spinal interneurons during CST detour circuit formation to show that neuronal activity guide the

---

[1]Institute of Clinical Neuroimmunology, University Hospital, Ludwig-Maximilians University Munich, Munich, Germany; [2]Biomedical Center, Medical Faculty, Ludwig-Maximilians University Munich, Martinsried, Germany; [3]Munich Cluster for Systems Neurology (SyNergy), Munich, Germany; [4]Graduate School of Systemic Neurosciences, Ludwig-Maximilians University Munich, Martinsried, Germany.

*P.M. Bradley and C.K. Denecke contributed equally to this paper; Correspondence to Florence M. Bareyre: florence.bareyre@med.uni-muenchen.de.

Rockefeller University Press
J. Exp. Med. 2019 Vol. 216 No. 11 2503–2514
https://doi.org/10.1084/jem.20181406

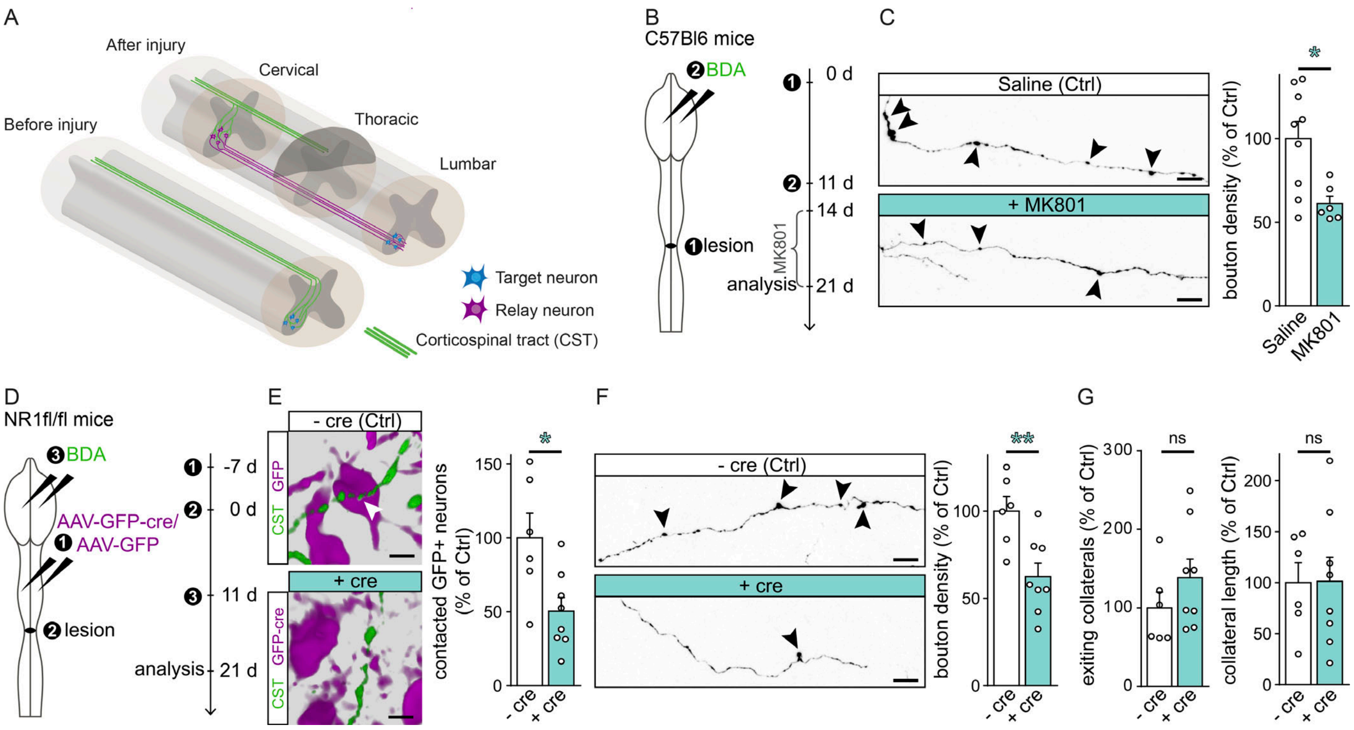

Figure 1. **Pharmacological inhibition and genetic ablation of NMDARs decreases CST-relay neuron contacts after SCI. (A)** Illustration of CST detour circuit formation following SCI. **(B)** Experimental setup of the pharmacological inhibition of NMDARs. **(C)** Confocal images and quantitative analysis of the number of boutons on hindlimb CST collaterals in the cervical spinal cord (arrowheads indicate boutons; P = 0.0113; *n* = 6–9 mice per group). **(D)** Experimental setup of the genetic ablation of NR1 subunit of NMDARs in spinal relay neurons. **(E)** 3D reconstructions of CST contacts on AAV-transfected neurons (CST, green; GFP$^+$ neurons, magenta; arrowheads indicate contacted cells) and quantification (P = 0.0168; *n* = 6–8 mice per group). **(F)** Confocal images of cervical CST collaterals and quantitative analysis of bouton density on CST collaterals (P = 0.0064; *n* = 6–8 mice per group; arrowheads indicate boutons). **(G)** Quantitative analysis of the number (left panel, P = 0.2584) and length (right panel, P = 0.9673; *n* = 6–8 mice per group) of these collaterals in the cervical spinal cord. Data analyzed using two-tailed unpaired *t* test and presented as mean ± SEM (*, P > 0.05; **, P < 0.01). Ctrl, control; ns, not significant. Scale bars, 10 µm in C, E, and F. MK801 data: one experiment. NR1 data: two independent experiments.

remodeling of neuronal circuits and the restoration of neurological function in the injured adult CNS.

Results and discussion

Pharmacological inhibition and genetic ablation of NMDARs decreases CST-relay neuron contacts after SCI

To probe the role of activity during post-injury axonal remodeling in the spinal cord, we first pharmacologically inhibited NMDARs using the noncompetitive antagonist MK801 (Fig. 1 B). Blockade of NMDAR function during the phase of synapse formation (days 14–21 after lesion) significantly decreased bouton density along sprouting CST collaterals (Fig. 1 C). To ascertain the specific contribution of postsynaptic NMDARs to de novo synapse formation, we ablated the NR1 subunit of the NMDAR in spinal interneurons by injecting a recombinant adeno-associated virus (rAAV) expressing GFP and the Cre recombinase (rAAV-GFP-Cre) or a control virus (rAAV-GFP) into the cervical spinal cord (C4 level) of NR1-floxed mice (Fig. 1 D; Tsien et al., 1996). Both viruses showed similar expression patterns in the spinal cord (rAAV-GFP-Cre: 147 ± 13 GFP$^+$ neurons/section and rAAV-GFP: 167 ± 8 GFP$^+$ neurons/section; *n* = 6–8 mice per group; Fig. S1 B). Cre expression resulted in a reduced proportion of GFP$^+$ (i.e., NR1-deficient) neurons contacted by CST collaterals (Fig. 1 E) as well as in a decrease in bouton density on cervical CST collaterals (Fig. 1 F) but did not affect the overall number or length of these collaterals (Fig. 1 G and Fig. S1 A). Our observation provides an interesting parallel to previous findings during developmental circuit formation (Iwasato et al., 2000; Washbourne et al., 2002; Ultanir et al., 2007) and indicates that the canonical function of NMDAR signaling during the formation of nascent synapses extends to the injured adult nervous system.

Inhibition of cyclic AMP response element-binding protein (CREB) activation alters remodeling of injured circuits

To better understand how signals downstream of NMDARs regulate circuit remodeling, we focused on the role of the transcription factor CREB, which is a critical checkpoint for activity-dependent synaptic strengthening (Flavell and Greenberg, 2008). We blocked CREB-dependent transcription in spinal relay neurons by injecting either an rAAV expressing aCREB, a dominant-negative inhibitor of CREB (Ahn et al., 1998) and GFP (rAAV-GFP-aCREB), or GFP alone (rAAV-GFP) into the cervical spinal cord (C4 level; Fig. 2 A). Both viruses showed a similar neuronal transduction pattern in the cervical spinal cord (rAAV-GFP-aCREB: 159 ± 8 GFP$^+$ neurons/section, rAAV-GFP: 148 ± 8 GFP$^+$ neurons/section, *n* = 6–8 mice per group; Fig. S1 D).

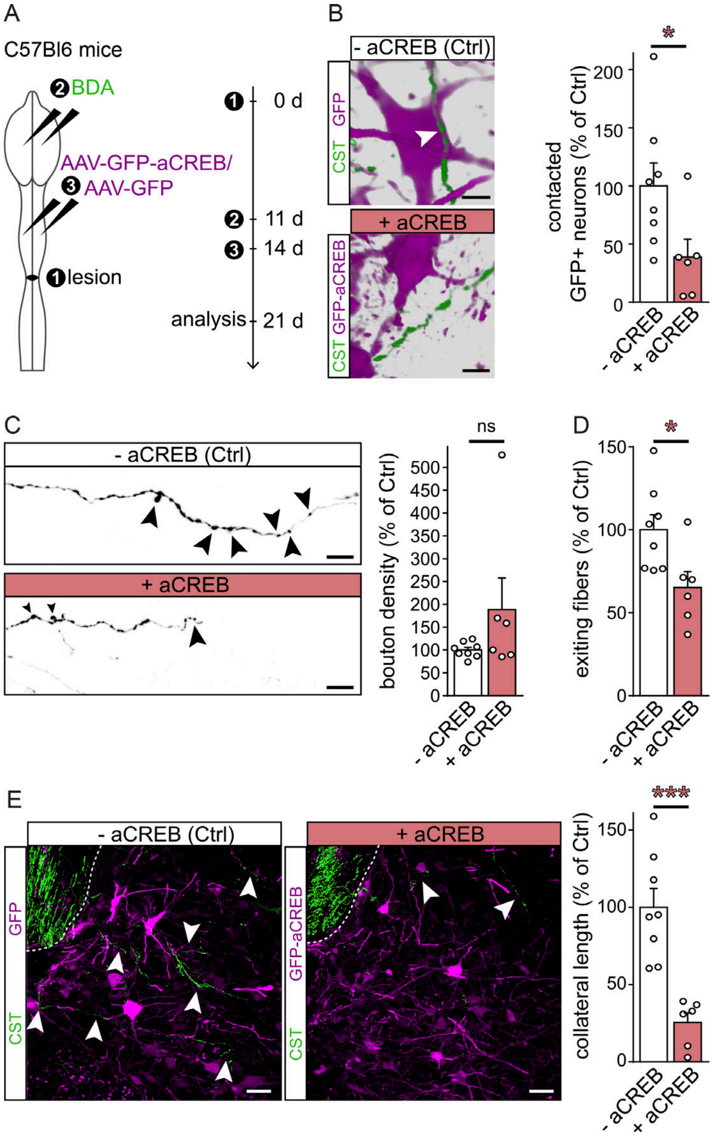

Figure 2. **Inhibition of CREB-mediated transcription alters remodeling of injured circuits. (A)** Experimental setup of the inhibition of CREB-mediated transcription using viral delivery of a dominant-negative inhibitor (aCREB). **(B)** 3D reconstructions of CST contacts on AAV-transfected neurons (CST, green; GFP$^+$ neurons, magenta; arrowheads indicate contacted cells) and quantification ($P = 0.0393$, n = 6–8 mice per group). **(C)** Confocal images of cervical CST collaterals and quantitative analysis of the bouton density on CST collaterals ($P = 0.1636$; n = 6–8 mice per group; arrowheads indicate boutons). **(D)** Quantitative analysis of the number ($P = 0.0229$, n = 6–8 mice per group) of these collaterals in the cervical spinal cord of mice injected with rAAV-GFP (−aCREB) or rAAV-GFP-aCREB (+aCREB). **(E)** Confocal images (left panel) of cervical CST collaterals (green) and aCREB-transduced neurons (magenta; arrowheads indicate CST collaterals) and quantitative analysis (right panel) of the length of CST collaterals ($P = 0.0004$, n = 6–8 mice per group). Data were analyzed using two-tailed unpaired t test and presented as mean ± SEM (*, $P < 0.05$; ***, $P < 0.001$). Ctrl, control; ns, not significant. Scale bars, 10 µm in B and C, and 50 µm in E. aCREB data: two independent experiments.

Subsequent analysis showed that inhibiting CREB activation during CST remodeling reduced the proportion of GFP$^+$ (and thus CREB-inhibited) neurons contacted by CST collaterals (Fig. 2 B). In contrast to NR1 ablation, inhibition of CREB activation did not affect the density of boutons on CST collaterals (Fig. 2 C) but rather their morphology (Fig. 2, D and E; and Fig. S1 C). As deletion of NMDARs on relay neurons had no such effect on CST collaterals, these findings suggest that maintaining NMDAR signaling, while interrupting the downstream activation of CREB in the postsynaptic neurons, can affect presynaptic axons.

Remodeling circuits but not mature spinal circuits are shaped by activity-dependent signals

We next investigated whether the observed changes were specific to remodeling circuits or whether mature circuits would also be affected by the perturbation of activity-dependent signaling in postsynaptic neurons. To determine the contribution of postsynaptic NMDARs to synapse maintenance in mature detour circuits, we ablated the NR1 subunit of the NMDAR in spinal interneurons after completion of circuit remodeling at 12 wk following injury (Fig. S2 A). In contrast to our previous results (Fig. 1), the delayed NMDAR depletion affected neither the number of CST-relay neuron contacts nor the bouton density on CST collaterals (Fig. S2, B–D).

We then blocked CREB activation in an unlesioned mature circuit, namely, the forelimb CST projection to the cervical spinal cord (Fig. S3 A). Our results showed that interfering with CREB-dependent transcription in the target neurons of the forelimb CST of healthy mice had no effect on the morphology and contact pattern of the CST collaterals (Fig. S3, B–E). These results support the concept that there is a specific time window of endogenous axonal remodeling after injury, during which neuronal activity can influence the remodeling of new circuits without affecting the preserved mature circuitry. These results are interesting to discuss in the context of recent studies demonstrating the importance of proprioceptive afferents for locomotor recovery after SCI (Takeoka et al., 2014; Takeoka and Arber, 2019). Consistent with our observations here, the authors show that the delayed ablation of proprioceptive afferents after maximal behavioral recovery (at 7 wk after injury) did not alter the remodeling of descending circuits, while such inputs are critical for instructing circuit reorganization at earlier stages of the recovery process. The existence of such a defined window of endogenous post-injury remodeling has obvious implications for the timing of therapies aimed at modulating neuronal activity that would be expected to be most beneficial if initiated during this time.

Activity-dependent competition shapes corticospinal remodeling after injury

A critical step in efficiently supporting post-injury circuit remodeling is to better understand the principles of contact selection, which ensure that functionally advantageous connections are formed and maintained while disadvantageous ones are removed. To do so, we used a designer receptor exclusively activated by designer drugs (DREADD)–based chemogenetic approach (Armbruster et al., 2007; Miao et al., 2015; Hilton et al., 2016) to chronically hyperpolarize relay neurons in the cervical cord (Roth, 2016; Chen et al., 2018; Mahler and Aston-Jones, 2018). Here we used this technique to perform the following sets of experiments. First, we coinjected a rAAV driving Cre-dependent expression of the hyperpolarizing DREADD hM4Di (rAAV-DIO-hM4Di-mCherry; Krashes et al., 2011) with an rAAV-GFP-Cre in the cervical spinal cord (C4 level) in order to suppress firing nonselectively, i.e., in both excitatory and inhibitory neurons (Fig. 3 A). We verified that our approach yielded similar neuronal transduction pattern (−clozapine-N-oxide [CNO]: 119 ± 8 GFP^+ neurons/section, +CNO: 119 ± 12 GFP^+ neurons/section; $n = 9$ mice per group; Fig. S1 F, left). Under these conditions, administration of CNO (which activates the hyperpolarizing receptor) during CST remodeling (from 14 to 21 d after SCI) did not affect the proportion of contacted GFP^+ cells (Fig. 3 B), the density of CST boutons (Fig. 3 C), or the length and number of exiting CST collaterals (Fig. 3 D and Fig. S1 E, top).

To more selectively silence the neuronal populations contacted by CST collaterals, we compared CST contact formation on inhibitory neurons (labeled in GlyT2-GFP mice) and excitatory interneurons (labeled in vGlut2-cre mice injected with a DIO-rAAV). This analysis revealed that while ∼6% of excitatory interneurons are contacted by CST collaterals, glycinergic neurons in the same location are almost never contacted (5.8 ± 1.47% contacted $vGlut2^+$ neurons versus 0.4 ± 0.06% contacted $GlyT2^+$ neurons; $P = 0.0003$, $n = 15$ GlyT2 and $n = 12$ VGlut2 mice). As excitatory spinal neurons are, thus, primarily contacted by emerging CST collaterals, we next selectively targeted $VGlut2^+$ neurons by injecting AAV-DIO-hM4Di-mCherry in the cervical spinal cord (C4 level) of VGlut2-Cre mice (Fig. 3 E; Vong et al., 2011). We first verified that the transduction patterns of rAAVs were similar in both groups (−CNO: 172 ± 9 $mCherry^+$ cells per section; +CNO: 174 ± 8 $mCherry^+$ cells per section, $n = 10–12$ mice per group; Fig. S1 F). In this selective silencing paradigm, CNO treatment now impacted detour circuit formation and resulted in a reduction of the proportion of $mCherry^+$ neurons contacted by CST collaterals (Fig. 3 F), an overall decreased bouton density on CST collaterals (Fig. 3 G), and altered collateral morphology (Fig. 3, H and I; and Fig. S1 E, bottom). To further investigate the role of neuronal activity for attracting and maintaining CST collaterals in the vicinity of relay neurons, we quantified the number of boutons on neurons that are contacted by a CST collateral. This analysis showed that the number of boutons per contacted neuron is decreased after neuronal silencing, indicating that when collaterals reach silenced neurons, they form fewer contacts (Fig. 3 K, left). Furthermore, the density of CST boutons on the stretch of the collateral that is in immediate apposition to the relay neuron is also reduced if the corresponding neurons are silenced (Fig. 3 K, right). Taken together, this indicates that neuronal activity is not required to attract CST collaterals to spinal interneurons or maintain them in apposition, but rather that it selectively affects the formation or stabilization of synapses onto these neurons.

We observe that global silencing of both excitatory and inhibitory interneurons does not affect circuit remodeling, whereas selective silencing of excitatory neurons—an intervention that reveals neuronal competition (Burrone et al., 2002; Tao and Poo, 2005)—alters circuit formation. Thus, our data now provide direct evidence that activity-dependent neuronal competition governs post-injury remodeling in the adult CNS. We next investigated whether relative differences in the extent of hyperpolarization between individual spinal relay neurons affected their probability to be contacted by sprouting CST collaterals. To achieve this, we measured the expression levels of DREADD-mCherry using three-dimensional (3D) surface rendering of >1,000 individual relay neurons in control and CNO-treated mice (Fig. 3 L). We could not observe a significant difference in general mCherry intensity between the control and treated groups (−CNO: median = 100% of control, +CNO: median = 110% of control; $n = 9{,}614$ and 8,449 neurons analyzed in −CNO and +CNO mice, respectively). However, while in the control group, neurons with a wide range of DREADD-mCherry expression were contacted by CST collaterals, the levels of DREADD-mCherry expression negatively correlated with the probability of those neurons to be contacted by growing CST collaterals in the CNO-treated group (Fig. 3 M; −CNO, $n = 1{,}198$ neurons; +CNO, $n = 368$ neurons analyzed). These results further support the notion that target selection during post-injury remodeling in the adult CNS is implemented by axonal competition based on postsynaptic relay neuron activity.

Next, to understand whether these selection rules are shared between all excitatory spinal interneurons or are specific to distinct neuronal subpopulations, we investigated CST contacts onto LPSNs, excitatory neurons that provide a detour to the lumbar spinal cord following injury (Bareyre et al., 2004; Jacobi et al., 2015). We retrogradely labeled these LPSNs by injecting Fluorogold into the projection area of LPSN in the lower thoracic spinal cord (level T12/L1). The results of this analysis showed that silencing all excitatory neurons leads to a reduction (54.8% of control) in CST contacts onto LPSNs (−CNO, $n = 7$; +CNO, $n = 5$ mice analyzed), similar to the reduction of CST contacts onto all $mCherry^+$ interneurons (34.3 ± 8.6% of control; see Fig. 3 F). This indicates that the activity dependent regulation of CST contact formation is likely shared between different excitatory interneuron populations.

Finally, to assess whether LPSNs compete with other excitatory neurons for CST input, we selectively silenced LPSNs. For

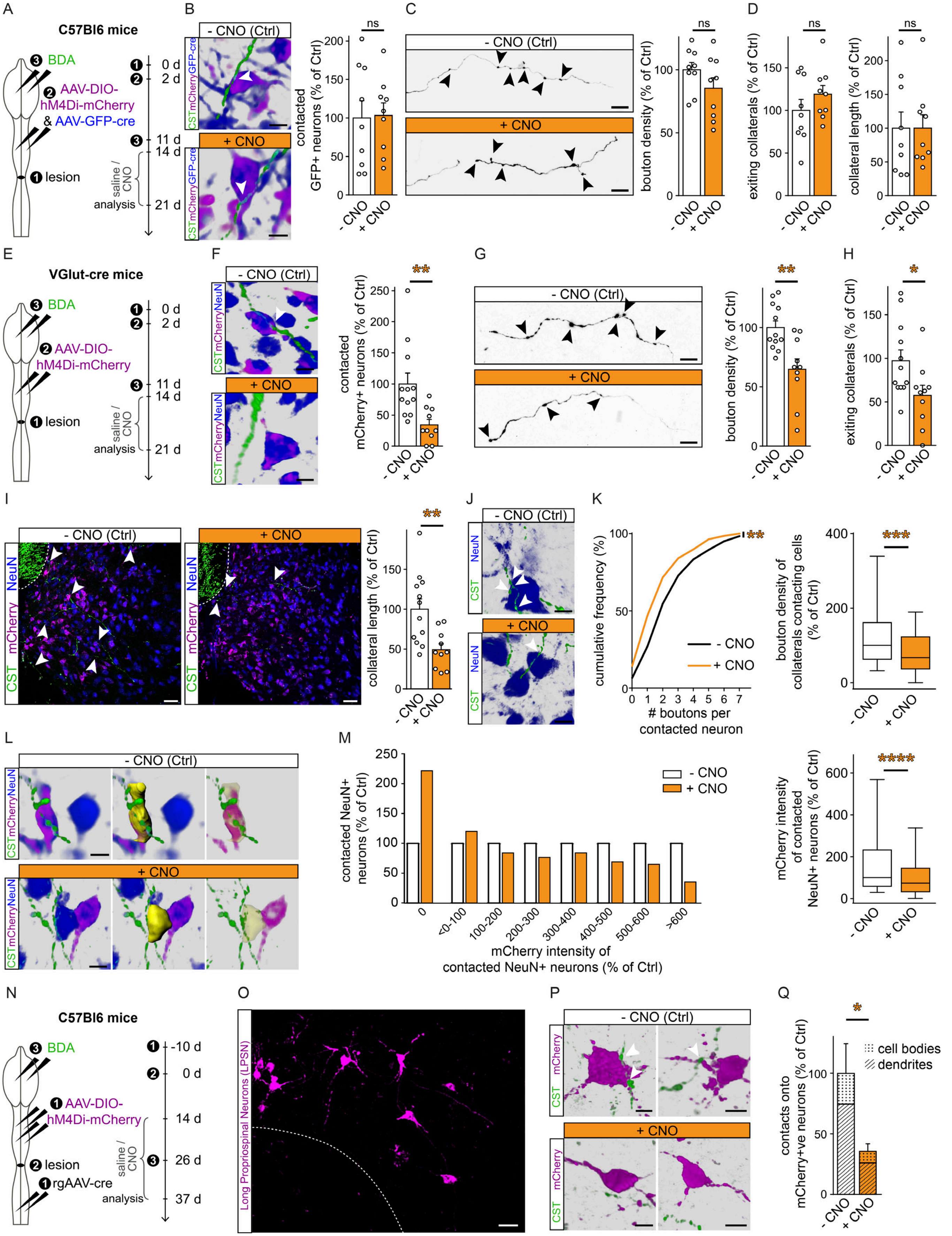
A
C57Bl6 mice
③ BDA
② AAV-DIO-hM4Di-mCherry & AAV-GFP-cre
① lesion
① 0 d
② 2 d
③ 11 d
14 d
saline / CNO
analysis
21 d
B
- CNO (Ctrl)
+ CNO
CST mCherry GFP-cre
contacted GFP+ neurons (% of Ctrl)
ns
- CNO
+ CNO
C
bouton density (% of Ctrl)
D
exiting collaterals (% of Ctrl)
collateral length (% of Ctrl)
E
VGlut-cre mice
② AAV-DIO-hM4Di-mCherry
F
CST mCherry NeuN
contacted mCherry+ neurons (% of Ctrl)
**
G
H
*
I
collateral length (% of Ctrl)
J
K
cumulative frequency (%)
boutons per contacted neuron
bouton density of collaterals contacting cells (% of Ctrl)
***
L
M
contacted NeuN+ neurons (% of Ctrl)
0
<0-100
100-200
200-300
300-400
400-500
500-600
>600
mCherry intensity of contacted NeuN+ neurons (% of Ctrl)
mCherry intensity of contacted NeuN+ neurons (% of Ctrl)
****
N
C57Bl6 mice
① -10 d
② 0 d
14 d
③ 26 d
37 d
① AAV-DIO-hM4Di-mCherry
② lesion
① rgAAV-cre
O
Long Propriospinal Neurons (LPSN)
P
CST mCherry
Q
contacts onto mCherry+ve neurons (% of Ctrl)
cell bodies
dendrites

Figure 3. **Activity-dependent competition shapes intraspinal remodeling after injury. (A)** Experimental setup used for silencing excitatory and inhibitory neurons based on viral delivery of DREADDs in C57Bl6 mice. **(B)** 3D reconstructions of CST contacts on AAV-transfected neurons (−CNO, treated with saline; +CNO, treated with CNO; CST, green; GFP$^+$ neurons, blue; DREADD-mCherry, magenta; arrowheads indicate contacted cells) and quantification ($P = 0.9079$, $n = 9$ mice per group). **(C)** Confocal images of cervical CST collaterals (arrowheads indicate boutons) and quantitative analysis of the bouton density on these collaterals ($P = 0.1651$; $n = 9$ mice per group). **(D)** Quantitative analysis of the number (left panel, $P = 0.2682$) and length (right panel, $P = 0.9980$; $n = 9$ mice per group) of CST collaterals in the cervical spinal cord of mice injected as described above. **(E)** Experimental setup used for selectively silencing excitatory neurons based on viral delivery of DREADDs in VGlut2-cre mice (see results in F–L). **(F)** 3D reconstructions of CST contacts on AAV-transfected neurons (−CNO, treated with saline; +CNO, treated with CNO; CST, green; NeuN$^+$ relay neurons, blue; DREADD-mCherry, magenta; arrowheads indicate contacted cells) and quantification ($P = 0.0049$, $n = 10$–12 mice per group). **(G)** Confocal images of cervical CST collaterals and quantitative analysis of the bouton density on these collaterals ($P = 0.0022$; $n = 10$–12 mice per group; arrowheads indicate boutons). **(H)** Quantitative analysis of the number of CST collaterals in the cervical spinal cord ($P = 0.0323$; $n = 10$–12 mice per group). **(I)** Confocal images (CST collaterals, green; DREADD-transduced neurons, magenta) and quantitative analysis of the length ($P = 0.0044$; $n = 10$–12 mice per group) of CST collaterals in the cervical spinal cord (arrowheads indicate CST collaterals). **(J)** 3D reconstructions of CST collaterals in direct vicinity of relay neurons (arrowheads indicate contacts). **(K)** Cumulative frequency distribution (left panel; −CNO, $n = 181$ contacted cells from seven mice analyzed; +CNO, $n = 138$ contacted cells from five mice analyzed) and bouton density of CST collaterals in direct apposition of contacted neurons (right panel; $P = 0.0001$, −CNO, $n = 181$ from seven mice; +CNO, $n = 138$ from five mice contacted cells analyzed). Box borders represent the 25th and 75th percentiles, whiskers 10th and 90th percentiles. **(L)** 3D reconstructions illustrating how the DREADD level within the spinal relay neurons contacted by CST collaterals is determined (CST, green; NeuN$^+$ neurons, blue; DREADD-mCherry, magenta; surface rendering, yellow). **(M)** Histogram (left panel) depicting the probability of relay neurons to be contacted by growing CST collaterals in relation to their expression levels of the DREADD constructs (+CNO, orange bars; −CNO, white bars) and box plot (right panel) showing the median intensity of DREADD expression in CST contacted relay neurons ($P < 0.0001$, −CNO, $n = 1{,}198$ from 12 mice; +CNO, $n = 368$ from 10 mice contacted cells analyzed). Box borders represent the 25th and 75th percentiles, and whiskers represent the 10th and 90th percentiles. **(N)** Experimental setup for selective silencing of LPSNs based on viral delivery of DREADDs in C57Bl6 mice. **(O)** Confocal images of the spinal cord to illustrate the location of LPSNs transduced with DREADDs (labeled by DREADD-mCherry, magenta). **(P and Q)** 3D reconstructions of CST contacts of rAAV-DIO-hM4Di-mCherry transduced neurons (P, −CNO, treated with saline; +CNO, treated with CNO; CST, green; DREADD-mCherry, magenta; arrowheads indicate contacts) and quantification (Q, $P = 0.0312$, $n = 7$ or 8 mice per group). CST contacts were evaluated onto cell bodies (dotted boxes) and dendrites (dashed boxes) revealing that CNO treatment reduced contact formation without affecting contact distribution (−CNO, 25.4% somatic versus 74.6% dendritic contacts, 134 contacts from eight mice; +CNO, 26.8% somatic versus 73.2% dendritic contacts, 41 contacts from seven mice). Data were analyzed using two-tailed unpaired t test for B–I and Q and presented as mean ± SEM, a Kolmogorov–Smirnov test for K, left, and with a Mann–Whitney test for K, right, and M, right. Ctrl, control. Scale bars, 10 µm in B, C, F, G, J, L, and P; 50 µm in I; and 100 µm in O. C57Bl6-DREADD data: two independent experiments. VGlut-DREADD data: two independent experiments. Analysis in K and Q was derived from one experiment. *, $P < 0.5$; **, $P < 0.01$; ***, $P < 0.001$; ****, $P < 0.0001$.

---

this purpose, we first injected a retrograde rAAV expressing the Cre recombinase into the lower thoracic spinal cord (level T12/L1), the target area of long propriospinal projections, and then injected an rAAV driving Cre-dependent expression of the hyperpolarizing DREADD hM4Di (rAAV-DIO-hM4Di-mCherry; Krashes et al., 2011) into the cervical spinal cord (level C4–C6; Fig. 3 N). This approach resulted in a similar number of LPSNs labeled in control and the CNO chronically treated group (−CNO: 11.8 ± 0.6 neurons/section, $n = 8$ mice; +CNO: 12.5 ± 0.6 neurons/section, $n = 7$ mice) that were distributed in the intermediate laminae of the spinal cord (Fig. 3 O; Jankowska et al., 1974; Alstermark et al., 1987; Bareyre et al., 2004). CNO treatment affected detour circuit formation and resulted in a significant reduction of the proportion of mCherry$^+$ neurons contacted by CST collaterals (35.7 ± 6% of control; Fig. 3, P and Q). Our results show that selective silencing of LPSNs led to a marked decrease of CST contacts onto both the cell bodies and dendrites of these cells, consistent with the idea that silencing puts them at a competitive disadvantage compared with the other excitatory interneurons in the spinal cord (Fig. 3 Q).

Activity-dependent shaping of corticospinal circuits limits motor recovery after SCI

To assess the consequences of interfering with activity-dependent competition for the functional recovery that spontaneously occurs following incomplete spinal cord lesions, we silenced excitatory relay neurons by injecting AAV-DIO-hM4Di-mCherry into the cervical spinal cord (level C4–C6) of lesioned VGlut2-Cre mice and chronically treated them with CNO (or vehicle solution) from 14 to 20 dpi (days post injury; Fig. 4 A). We then monitored the gait recovery of the mice using Catwalk (Hamers et al., 2006) and quantified gait characteristics of stepping movements during the recovery period (≤21 dpi, 24 h after the last drug injection) following administration of CNO or vehicle. Due to the large number of parameters (177) analyzed by the Catwalk software, we performed a principal component analysis (PCA) to reduce dimensionality and provide a comprehensive quantification of locomotor features (Courtine et al., 2009). We visualized gait patterns in the two-dimensional coordinates created by PC1–2, where PC1 explains the highest variance (30.5%) and separates the CNO versus vehicle treatment group (Fig. 4 B). More specifically, the mean values of PC1 scores at 21 dpi of mice treated with CNO were significantly different from those of vehicle-treated mice (Fig. 4 C). Furthermore, while mice treated with vehicle recovered the locomotion features captured by PC1 at 21 dpi and reached levels close to unlesioned mice, animals treated with CNO did not show a significant recovery compared with the acute injury stage (at 3 dpi; Fig. 4 D). The distinct characteristics captured by component 1 were extracted from the analysis of factor loadings and grouped into functional clusters (Fig. 4 E). Factor loading revealed that several parameters related to gross locomotion, interlimb coordination, hindlimb paw print shape, or the timing of paw placement were highly correlated to PC1 and explained the lack of recovery following CNO treatment (Fig. 4 E).

Taken together these results indicate that the activity-dependent shaping of circuit remodeling enables efficient recovery of motor function after SCI. Strategies that enhance

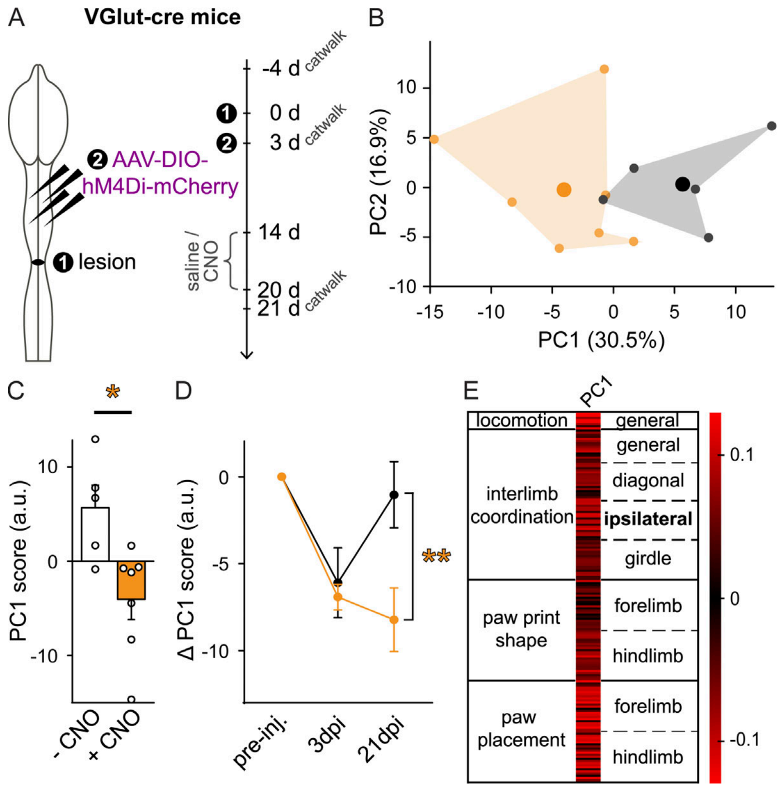

Figure 4. **Silencing of relay neurons impairs gait recovery after SCI. (A)** Experimental setup used for analyzing the impact of silencing excitatory relay neurons on motor recovery. **(B)** Two-dimensional statistical representation of gait parameters after performing PCA. Each small colored dot represents the gait pattern from an individual mouse chronically treated (orange) or nontreated (black) with CNO (n = 5–7 mice per group). Big dots represent the group mean. **(C)** Bar graphs of average scores on principal components 1 at 21 dpi after injury (P = 0.0140; n = 5–7 mice per group; mean ± SEM). **(D)** Line graph showing the relative changes of PC1 compared with preinjury levels over the time course of the experiment (P = 0.0021; n = 5–7 mice per group; mean ± SEM). **(E)** Color-coded representation of factor loadings that identify each parameter's correlation coefficient (r) with PC1. Parameters with positive/negative correlation are coded in red, while those with a correlation close to 0 are coded in black (see scale below). Data on PC1 were analyzed with a t test in C and with a repeated two-way ANOVA followed by a Bonferroni post hoc test in D. Behavioral analysis: one experiment. a.u., arbitrary units; pre-inj., pre-injury. *, $P < 0.05$; **, $P < 0.01$.

physiological activity patterns of relay neurons based on optogenetic or chemogenetic approaches, electrical stimulation, or rehabilitative measures might thus be harnessed to strengthen corticospinal connectivity and improve functional recovery after CNS injuries.

Materials and methods

Animals

To suppress firing in excitatory spinal cord interneurons, we injected cre-dependent DREADD vectors into VGlut2-Cre mice (Vong et al., 2011; The Jackson Laboratory; 6J.129S6(FVB)-Slc17a6tm2(cre)Lowl/MwarJ), in which Cre expression is restricted to neurons expressing the endogenous vesicular glutamate transporter 2, the primary vesicular glutamate transporter in excitatory neurons of the spinal cord. To delete the NR1 subunit of the N-methyl-D-aspartate receptor from spinal cord interneurons, we injected rAAV-GFP-IRES-Cre into floxed NR1 mice (Tsien et al., 1996; The Jackson Laboratory; B6.129S4-Grin1tm2Stl/J). To determine contacts between corticospinal collaterals and glycinergic inhibitory interneurons, we used GlyT2-GFP mice (Zeilhofer et al., 2005). For all other experiments, we used adult female C57/Bl6 mice (6–12 wk old). All animal experiments were performed in accordance with regulations of the animal welfare act and protocols approved by the Regierung von Oberbayern.

Generation and production of rAAV vectors

pAAV-GFP-IRES-Cre (rAAV-GFP-IRES-Cre) was created as described previously (Jacobi et al., 2015). pAAV-GFP (rAAV-GFP) was created by inserting enhanced GFP (EGFP; from pEGFPN1) at the HincII site of pAAV-CMV-MCS. pAAV-hSyn-DIO-hM4D(Gi)-mCherry was a gift from B. Roth (University of North Carolina, Chapel Hill, Chapel Hill, NC). pAAV-CMV-eGFP-T2A-aCREB (rAAV-GFP-aCREB) was a gift from H. Gainer (National Institute of Neurological Disorders and Stroke, National Institutes of Health, Bethesda, MD).

rAAV chimeric virions containing a 1:1 ratio of AAV1 and AAV2 capsid proteins and the gene of interest were generated as previously described (Jacobi et al., 2015). Genomic titers were as follows: rAAV-GFP, 3 × 10^{10} genome copies/ml; rAAV-hSyn-DIO-hM4D(Gi)-mCherry, 2.2 × 10^{11} genome copies/ml; rAAV-eGFP-T2A-aCREB, 6.8 × 10^{10} genome copies/ml; and rAAV-GFP-IRES-Cre, 1.0 × 10^{10} genome copies/ml.

The following viruses were purchased from Addgene: rAAV2-hSyn-DIO-hM4Di(Gi)-mCherry (titer: 1.9 × 10^{13} genome copies/ml; catalog no. 44362-AAV2), rAAV8-hSyn-DIO-hM4Di(Gi)-mCherry (titer: ≥1 × 10^{13} genome copies/ml; catalog no. 44362-AAV8), and rAAV2-pmSyn1-eBFP-cre (titer: 5 × 10^{12} genome copies/ml; catalog no. 51507-AAVrg).

Surgical procedures

Mid-thoracic dorsal hemisection

Mice were anesthetized with a subcutaneous injection of ketamin/xylazine (100 mg/kg ketamine and 13 mg/kg xylazine). After a laminectomy at thoracic level 8 (T8), a mid-thoracic dorsal hemisection, which results in a bilateral transection of the main dorsal and minor dorso-lateral CST component but leaves the ventral white matter intact, was performed with fine iridectomy scissors (Bareyre et al., 2004; Lang et al., 2013). Prior to and after surgery, animals were kept on a heating pad (38°C). Mice were sacrificed 3, 5, or 12 wk after dorsal hemisection.

Labeling of hindlimb CST fibers

The hindlimb CST was traced by bilateral 1 µl injections of a 10% (in 0.1 M phosphate buffer) solution of biotinylated dextran amine (BDA; 10,000 daltons, molecular weight; Life Technologies) using fine pulled glass micropipettes, 10 d before the sacrifice date (coordinates from bregma: −1.3 mm caudal, 1.2 mm lateral, and 0.6 mm depth).

Labeling of forelimb CST fibers

10 d before sacrifice, 0.5 µl of a 10% (in 0.1 M phosphate buffer) solution of BDA was injected into the right forelimb motor cortex (coordinates from bregma: −0.6 mm caudal, 1 mm lateral, and 0.6 mm depth) using fine pulled glass micropipettes.

Labeling of LPSN with Fluorogold

10 d before sacrifice, 0.5 µl of Fluorogold (1% in 0.1 M Cacodylate buffer; Fluorochrome) was injected at T12/L1 (coordinates from midline: 0.3 mm lateral and 0.6 mm depth) using fine pulled glass micropipettes.

Manipulation of neuronal activity

Pharmacological NMDAR blockade

Starting 14 d after lesion, animals were randomized into control and treatment groups and received once-daily i.p. injections of either saline or MK801 (0.25 mg/kg diluted in saline; Tocris Bioscience; Kakizawa et al., 2000) until sacrifice at day 21 after lesion (no animals were excluded from the analysis). Tracking the movement of mice in an open field confirmed that at this dose, MK801 did not produce any sedation; rather, animals showed a transient increase in their locomotor activity that resolved after 2 h (between 0 and 30 min +MK801: 254.1 ± 35.2% of control's distance traveled; between 120 and 150 min +MK801: 108.9 ± 11.4% of control's distance traveled).

NR1 deletion

rAAV-GFP-IRES-Cre or control rAAV-GFP was injected into the cervical spinal cord of floxed NR1 mice at the C4 level (0.5 µl rAAV injected bilaterally; coordinates from midline: 0.4 mm lateral and 0.7 mm depth). For NR1 deletion during detour circuit formation (Fig. 1), rAAVs were injected 7 d before the lesion, and animals were then sacrificed at 21 d after lesion. To assess the effect of NR1 KO on the mature hindlimb detour circuit (Fig. S2), animals were injected with rAAVs at 8 wk and sacrificed at 12 wk after lesion, respectively.

Inhibition of CREB-mediated transcription

rAAV-eGFP-T2A-aCREB (Ahn et al., 1998) or control rAAV-GFP was injected bilaterally into the cervical spinal cord of C57Bl6 mice as described above. To assess effects of blocking CREB activation on detour circuit formation (Fig. 2), animals were injected with rAAVs at 14 d and sacrificed at 21 d after lesion, respectively. To assess effects of CREB blockade on the mature unlesioned forelimb CST projection (Fig. S3), rAAVs were injected into the cervical spinal cord (C4) of unlesioned mice 7 d before sacrifice. The cervical spinal cord sections of all mice injected with AAVs using a CMV promoter were controlled for glial labeling, and the few sections in which labeled glial cells were apparent were excluded from the analysis.

Activity modulation using DREADDs

2 d after a spinal cord lesion, either a mix of rAAV-GFP-IRES-Cre and rAAV-hSyn-DIO-hM4D(Gi)-mCherry in PBS (C57Bl6 mice; Fig. 4, A–D) or rAAV-hSyn-DIO-hM4D(Gi)-mCherry (VGlut2-Cre mice; Fig. 4, E–M) was injected bilaterally at C4 for histological studies.

To modulate activity specifically in LPSN (C57Bl6 mice; Fig. 3), four injections of rAAV-hSyn-DIO-hM4D(Gi)-mCherry, spanning C4 to C6, were performed in mice that had received bilateral injections at T12/L1 (coordinates from midline: 0.3 mm lateral and 0.6 mm depth) of a retrograde rAAV-hSyn-eBFP-cre 10 d before the thoracic hemisection.

For behavioral studies, four injections of rAAV-hSyn-DIO-hM4D(Gi)-mCherry (in VGlut2-Cre mice; Fig. 4) were made between C4 and C6 in an alternating pattern (right/left) to maximize the number of interneurons silenced.

For all DREADD experiments, the mice were randomized into control and treatment groups at 14 d after lesion and received subcutaneous injections of either saline or CNO (1 mg/kg diluted in saline; Sigma-Aldrich) twice daily until sacrifice (Figs. 3 and 4).

Tissue processing

Tissue processing

Brains and spinal cords were dissected and post-fixed overnight in paraformaldehyde, then transferred to 30% sucrose/PBS solution for 2 d. 50-µm-thick coronal sections of the cervical enlargement were cut using a cryostat, collected, and processed free-floating. To visualize CST collaterals, the BDA signal was amplified by incubation with ABC Complex (Vector Laboratories) overnight at 4°C. After a 30-min tyramide amplification (Biotin-XX; TSA Kit 21; Life Technologies), sections were incubated overnight with streptavidin-conjugated Alexa Fluor 647 or streptavidin-conjugated Alexa Fluor 594 (1:500; Life Technologies).

Immunohistochemistry

All antibodies were incubated at 4°C overnight. In cases where rAAV-mediated expression of GFP was restricted to 7 d, the GFP signal was amplified using an anti-GFP antibody (A11122; Life Technologies) followed by a goat anti-rabbit-488 secondary antibody (both 1:500; Life Technologies). For experiments involving pAAV-hSyn-DIO-hM4D(Gi)-mCherry, staining with a mouse anti-NeuN antibody (MAB377; Millipore) followed by a goat anti-mouse-488 secondary antibody (both 1:500; Life Technologies) was used to label neuronal somata.

Image acquisition

Samples were coverslipped with Vectashield (Vector Laboratories), and all images were acquired at room temperature. Automated confocal scanning of spinal cord tissue was performed with the FV10-ASW microscopy software on an upright Olympus FV1000 confocal microscope system. Images were acquired using standard filter sets, and acquisition settings were kept constant between control and treatment groups for each experiment.

Spinal cord gray matter image acquisition

To analyze CST collateral length, bouton density, number of virally infected cells, and CST-relay neuron contacts, two confocal z-stacks per tissue section (one image for each side of the spinal cord) were acquired at 20× magnification (objective: Olympus UPLSAPO 20XO, imaging medium: Olympus IMMOIL-F30CC, NA [numerical aperture]: 0.85; 640 × 640 pixels, zoom 1.1×, 0.45 µm z-resolution, 16 bit) for up to 40 images (20 sections). Image fields of view were positioned so that their medial borders aligned with the spinal cord midline. The dorsal border was then set to include the entire CST. At this magnification, almost all of the ventral and lateral extent of the ventral gray matter was included, allowing the detection of all CST collaterals that preferentially project to this region.

CST tract image acquisition

To analyze the number of exiting fibers and the number of BDA-labeled CST tract fibers, image fields of view were centered on the CST tract so that all fluorescently labeled CST tract fibers as well as a sufficiently large area of the gray matter bordering the CST were included. Images were acquired at 20× magnification (objective: Olympus UPLSAPO 20XO, imaging medium: Olympus IMMOIL-F30CC, NA: 0.85; 640 × 640 pixels, zoom 1.1×, 0.45 µm z-resolution, 16 bit).

Image acquisition to assess distribution of viral transduction

Images covering the entire spinal cord cross-section were acquired using an upright Leica DM4 B microscope with a QImaging EXI camera at 5× magnification (objective: Leica HC PL FLUOTAR 5X, imaging medium: air, NA: 0.15; 1,392 × 1,040 pixels, zoom 1×; Fig. S1).

Image processing

For presentation purposes, images of collateral boutons were rescanned at 20× magnification (Kalman integration: 2, NA: 0.85, 1,024 × 1,024 pixels, zoom 1.1×, 0.45 µm z-resolution, 16 bit) and converted to 8-bit grayscale before application of an inverted look-up table. Exiting collateral images were also converted to 8-bit grayscale before application of an inverted look-up table. The individual images for the LPSN infection overview (Fig. 3 E) were scanned at 20× magnification (NA: 0.85; 1,024 × 1,024 pixels, zoom 1.0×, 0.45 µm z-resolution, 16 bit) and later stitched in Fiji with the Grid/Collection plugin. The BDA channel was subtracted from the LPSN channel to reduce background from spectral overlap and lipofuscin.

Figures depicting collateral–neuronal contact or gray matter collateral sprouting were pseudocolored in Imaris (Bitplane) or Fiji, respectively. For image display, gamma adjustments were made in Photoshop and Imaris to enhance visibility of intermediate gray values.

Histological analysis

All analyses were performed with the experimenter blinded with respect to control and treatment groups. Between 10 and 20 spinal cord sections, at level C4, where AAVs were injected, were analyzed per animal for all experiments. All analyses on maximum intensity projections were performed in Fiji. All analyses on 3D image stacks were performed in Imaris. All data are expressed as percentages of control values.

Quantification of BDA labeled CST tract fibers

To correct for variations in the efficiency of BDA labeling between animals, the average number of BDA$^+$ CST fibers in the dorsal column was determined in each animal. Briefly, a z-stack consisting of 15 images that was representative of the tract as a whole was used for evaluation. The border of the CST tract region, visible by tissue autofluorescence, was outlined using the freehand selection tool and the area outside set to a gray value of zero. The "Analyze tubeness" plugin in Fiji was then applied to identify axonal structures in a nonbiased, automated fashion. The number of structures (fibers) for each image was determined automatically using the "3D Objects Counter" plugin. The results from at least three images were averaged. Non-axonal fluorescent structures were either outlined and set to zero pixel intensity or, if too complex, the image was excluded from the analysis.

Sprouting CST collateral length

Up to 40 confocal z-stacks were converted to 8-bit maximum projections, and all BDA$^+$ collateral fragments present in the gray matter were traced in a semi-automated fashion in Fiji using the plugin "NeuronJ." The total length of CST collaterals per section was calculated and normalized to the number of labeled CST axons.

Bouton density on CST collaterals

The number of bouton-like structures present on CST collaterals was assessed for up to 40 maximally projected 16-bit z-stacks. Boutons were identified by their brightness, size, and rounded shape profile in relation to locally adjacent axonal structure. More precisely, blinded observers were trained to recognize boutons visually if the bouton's maximum intensity was about three times brighter (pixel value) or was at least about two times bigger (maximum Feret diameter) than their adjacent collateral. These criteria were later confirmed by intensity and size measurements in Fiji in a subset of boutons (n = 122 boutons analyzed). The total number of boutons per section was counted and expressed as number of boutons per length (bouton density). Finally, in order to ascertain that these CST boutons are indeed synapses, we double-stained a subset of sections containing labeled CST collaterals with the synaptic marker synapsin-1 (diluted 1:500; AB1543; Millipore; revealed with a secondary donkey anti-rabbit IgG antibody coupled with DyLight 405 diluted 1:100; Jackson Immunoresearch). Indeed, we found that >70% of the CST boutons visually identified based on the criteria listed above were synapsin-1–positive (70.8 ± 8.5% based on the analysis of >80 boutons from seven control mice at 3 wk after a thoracic spinal cord lesion). This is in accordance with our previous analysis of CST collaterals at this stage of the remodeling process (Jacobi et al., 2015).

Quantification of exiting CST collaterals

30 image stacks were analyzed per animal using Imaris. Briefly, images were examined in 3D, and the number of collaterals that

exited and, therefore, crossed the border of the CST tract into the spinal cord gray matter was counted. As BDA labeling of the mature forelimb projection was too dense to analyze exiting collaterals in an entire stack, sub-stacks of 10 planes were analyzed. The total number of exiting collaterals was normalized to the number of labeled CST axons.

Assessment of viral gene transfer in the spinal cord

The number of fluorescently labeled neurons per image was counted manually on maximum intensity projection image stacks. The data were then expressed as the number of positive cells per spinal cord section.

Analysis of the distribution of virally transduced interneurons in the spinal cord

Images of entire spinal cord cross-sections were registered using an Adobe Photoshop template with the central canal positioned in the middle and the section rotated accordingly (four animals per group and three sections per animals were overlaid). Then coordinates of transduced cells were determined in Fiji and used to create topographic maps in Python. Topographic maps were registered onto a spinal cord template (with white and gray matter borders) using a spinal cord atlas (Watson et al., 2009).

Assessment of retrograde viral gene spread to the brain

To ensure that rAAVs injected into the cervical spinal cord only targeted local interneurons and did not spread retrogradely to cortical projection neurons, we confirmed that no viral labeling of neurons was observed in the cortex (sections were analyzed from 300 µm rostral to 300 µm caudal of motor cortex injection coordinates for at least three mice per experimental group).

Quantification of contacts by collaterals onto GFP-labeled spinal cord neurons

20 image stacks per animal were assessed in 3D using Imaris software in "blend" mode to detect all putative contacts between collateral boutons and the cell bodies and proximal dendrites of GFP-expressing spinal cord gray matter neurons. To focus our analysis onto the cell body and the proximal dendrites, a median filter (3 × 3 × 3) was applied to the GFP channel to minimize signal from fine dendritic processes. To determine whether close appositions were true contacts, we used the following criteria. First, a bouton-like structure had to be present along the part of the CST collateral that was in immediate contact with the spinal relay neuron. Second, taking advantage of the inherent point spread present in confocal images, this CST bouton had to clearly overlap with the postsynaptic neuron. Each contacted neuron was marked once using the "measurement points" function. The number of contacts per section was calculated and normalized to the number of labeled axons in the CST tract and the average number of GFP$^+$ cells per section. As BDA labeling of the mature forelimb projection (Fig. S3) was too dense to analyze contacts in an entire stack, image stacks were reduced in the z-plane to 10 planes, with each image cropped at the same z-level and analyzed as described above. To ascertain that the 3D-Imaris analysis correctly identifies contacts, we verified the results of the 3D analysis on corresponding single confocal planes (0.45 µm z-resolution) imaged with high resolution (pixel size ≈0.9 µm) on a sample dataset (100% of contacts identified in the 3D analysis were verified on single confocal sections in Fiji, 137 contacts analyzed from seven animals).

Analysis of contacts onto DREADD$^+$ neurons in Vglut2-Cre mice

DREADD$^+$ neurons were identified based on the expression of the mCherry tag. NeuN immunohistochemistry was used to provide a structural marker of neuronal somata and proximal dendrites to enable contact analysis on cells irrespective of their mCherry intensity. Contacts onto all NeuN$^+$ neurons were then analyzed using the criteria described above. To identify DREADD$^+$ neurons within the contacted group, the mean intensity of DREADD-mCherry inside each contacted neuron was measured, and the tissue background was subtracted (see below).

Analysis of contacts onto cell bodies and dendrites of DREADD$^+$ LPSNs

To include dendrites in the analysis of contacts onto DREADD$^+$ LPSN, we used a Fiji-based analysis. First potential contacts were identified on maximum projections. Afterward, the experimenter went through individual z-images in the stack to confirm or refute an apposition of an LPSN cell body or dendrite (mCherry channel) with a varicosity on the CST collateral (BDA channel).

Measurement of DREADD levels in contacted spinal neurons

Using the "Marching cubes" setting in the Imaris "Surfaces" function, closed rendered surfaces were individually created in the NeuN channel for all contacted neurons to allow for measurements of mean mCherry pixel intensity per neuronal somatic volume.

mCherry background measurement

Mean tissue background intensity levels in the mCherry channel were determined for each animal by defining regions of interest in Fiji for five different average intensity–projected image stacks per animal, in regions of the gray matter devoid of mCherry$^+$ cells or processes.

Gait analysis

Gait was assessed using the Catwalk XT (Noldus; Hamers et al., 2006) ≥1 d following the last injection of CNO to ensure that no residual neuronal silencing from either CNO or metabolized clozapine would affect the behavioral testing (Chen et al., 2018). For data collection, all animals were familiarized with the system three times before preinjury acquisition. For each animal, three valid runs for each time point (preinjury, 3 dpi and 21 dpi) were recorded. A run was considered valid if it fulfilled the requirements preset in the system, a minimum run duration of 0.5 s, a maximum run duration of 4 s, and a maximum speed variation of 60%, to ensure that the animal walked on the runway without interruptions.

Catwalk generated 177 parameters that provide a detailed description of the gait of each animal under the given treatments. To reduce dimensionality in these datasets, we used a multivariate statistical analysis, PCA (Courtine et al., 2009). PCA is a mathematical transformation that converts the original dataset to a new coordinate system, such that the variance is maximized on each new coordinate axis. Due to a different scale of each parameter in the Catwalk analysis, 21 dpi data were first scaled to achieve unit variance. We next performed a PCA using the online software ClustVis (Metsalu and Vilo, 2015). The first two principal components were sufficient to account for ~50% of the total variance of the studied samples, demonstrating the high correlation between the variables describing gait. To visualize the differences between mice and the CNO treatment, we plotted coordinates from each mouse in the new space created by the first two principal components (Fig. 4 B). We then measured the average score of PC1 for 21 dpi (Fig. 4 C). Subsequently, we applied determined factor loadings and the 21 dpi unit variance scaling to the remaining time points (preinjury and 3 dpi) to calculate the relative changes of each animal's PC score (Fig. 4 D). The analysis of factor loadings was also presented to illustrate the correlations between distinct aspects of locomotion and principal component 1 (Fig. 4 E). In this representation, variables that correlate positively or negatively with a given principal component identified clusters of parameters that account for a specific difference between conditions due to CNO treatment (red colors indicate higher positive or negative correlation).

To assess the behavioral effect of MK801 injections, we performed open field recordings, starting immediately after a MK801 or saline i.p. injection until 180 min after injection. Distance traveled of each animal was recorded in 30-min intervals using the automated tracking software Any-maze (version 4.99).

Statistical analysis

Results are given as mean ± SEM with the exception of Fig. 3, K and M (medians; see below). All datasets were analyzed in Prism 7.00 for Windows (GraphPad Software). Normality was evaluated using the D'Agostino–Pearson omnibus normality test in Prism. When data followed a normal distribution, we used a two-tailed unpaired *t* test, and data were normalized to the controls mean. When data did not distribute normally, we used a Mann–Whitney test (Fig. 3 K, right; Fig. 3 M, right) or Kolmogorov–Smirnov (Fig. 3 K, left), and data were normalized to the controls median. Data with Mann–Whitney test are presented as a box-and-whisker plot representing the medians; box borders represent the 25th and 75th percentiles, whiskers the 10th and 90th percentiles. Data with a Kolmogorov–Smirnov test are presented with a cumulative distribution with an upper limit where the experimental group reaches 100%. Behavioral experiments were analyzed with a repeated two-way ANOVA followed by Bonferroni post hoc test (Fig. 4 D). To exclude animals in which abnormal forelimb labeling occurred due to incorrect BDA injection placement, data were analyzed for statistical outliers using the robust regression and outlier test in Prism (Q = 1%). Out of the entire study, only four animals were outliers and were therefore excluded from the study. Significance levels are indicated as follows: *, $P < 0.05$; **, $P < 0.01$; ***, $P < 0.001$; and ****, $P < 0.0001$.

Online supplemental material

Fig. S1 shows examples of exiting CST collaterals corresponding to quantifications shown in Figs. 1, 2, and 3. In addition, the distribution of rAAV-transduced neurons within the spinal cord in the different experiments is depicted. Fig. S2 shows the results of the experiment, in which we genetically ablated the NR1 subunit in spinal neurons at 12 wk after injury. While the same intervention performed during the ongoing remodeling process altered circuit formation, this analysis indicates that circuits that have completed the remodeling process are no longer sensitive to this manipulation. In line with these results, Fig. S3 shows that the inhibition of CREB-mediated transcription does not affect the circuit structure of the uninjured CST forelimb projections.

Acknowledgments

We thank L. Schödel and M. Adrian for technical assistance and D. Matzek and B. Stahr for animal husbandry. We thank D. Kerschensteiner for critical reading of the manuscript and C. Lang for the analysis of GlyT2-GFP mice.

Work in F.M. Bareyre's laboratory is supported by grants from the Deutsche Forschungsgemeinschaft (SFB 870 and SyNergy; EXC 2145), the Munich Center for NeuroSciences, and the Wings for Life foundation. Work in M. Kerschensteiner's laboratory is financed via the Deutsche Forschungsgemeinschaft (Transregio 128 and SyNergy; EXC 2145), the European Research Council (FP/2007-2013# 310932), the Bundesministerium für Bildung und Forschung, the Deutsche Multiple Sklerose Gesellschaft, and the "Verein Therapieforschung für MS-Kranke e.V."

The authors declare no competing financial interests.

Author contributions: P.M. Bradley, C.K. Denecke, M. Kerschensteiner, and F.M. Bareyre designed the experiments. P.M. Bradley and C.K. Denecke performed surgeries, histology, microscopy, and image and data analysis. A. Aljovic and C.K. Denecke performed behavior and analysis. C.K. Denecke designed the figures. A. Schmalz generated viruses. P.M. Bradley, C.K. Denecke, M. Kerschensteiner, and F.M. Bareyre wrote the paper.

Submitted: 24 July 2018
Revised: 10 May 2019
Accepted: 17 July 2019

References

Ahn, S., M. Olive, S. Aggarwal, D. Krylov, D.D. Ginty, and C. Vinson. 1998. A dominant-negative inhibitor of CREB reveals that it is a general mediator of stimulus-dependent transcription of c-fos. *Mol. Cell. Biol.* 18:967–977. https://doi.org/10.1128/MCB.18.2.967

Alstermark, B., A. Lundberg, L.-G. Pettersson, B. Tantisira, and M. Walkowska. 1987. Motor recovery after serial spinal cord lesions of defined descending pathways in cats. *Neurosci. Res.* 5:68–73. https://doi.org/10.1016/0168-0102(87)90024-1

Arakawa, H., A. Suzuki, S. Zhao, V. Tsytsarev, F.-S. Lo, Y. Hayashi, S. Itohara, T. Iwasato, and R.S. Erzurumlu. 2014. Thalamic NMDA receptor function is necessary for patterning of the thalamocortical somatosensory map and for sensorimotor behaviors. *J. Neurosci.* 34:12001–12014. https://doi.org/10.1523/JNEUROSCI.1663-14.2014

Armbruster, B.N., X. Li, M.H. Pausch, S. Herlitze, and B.L. Roth. 2007. Evolving the lock to fit the key to create a family of G protein-coupled receptors potently activated by an inert ligand. *Proc. Natl. Acad. Sci. USA.* 104:5163–5168. https://doi.org/10.1073/pnas.0700293104

Bareyre, F.M., M. Kerschensteiner, O. Raineteau, T.C. Mettenleiter, O. Weinmann, and M.E. Schwab. 2004. The injured spinal cord spontaneously forms a new intraspinal circuit in adult rats. *Nat. Neurosci.* 7: 269–277. https://doi.org/10.1038/nn1195

Buffelli, M., R.W. Burgess, G. Feng, C.G. Lobe, J.W. Lichtman, and J.R. Sanes. 2003. Genetic evidence that relative synaptic efficacy biases the outcome of synaptic competition. *Nature.* 424:430–434. https://doi.org/10.1038/nature01844

Burrone, J., M. O'Byrne, and V.N. Murthy. 2002. Multiple forms of synaptic plasticity triggered by selective suppression of activity in individual neurons. *Nature.* 420:414–418. https://doi.org/10.1038/nature01242

Chen, B., Y. Li, B. Yu, Z. Zhang, B. Brommer, P.R. Williams, Y. Liu, S.V. Hegarty, S. Zhou, J. Zhu, et al. 2018. Reactivation of dormant relay pathways in injured spinal cord by KCC2 manipulations. *Cell.* 174: 521–535.e13. https://doi.org/10.1016/j.cell.2018.06.005

Courtine, G., B. Song, R.R. Roy, H. Zhong, J.E. Herrmann, Y. Ao, J. Qi, V.R. Edgerton, and M.V. Sofroniew. 2008. Recovery of supraspinal control of stepping via indirect propriospinal relay connections after spinal cord injury. *Nat. Med.* 14:69–74. https://doi.org/10.1038/nm1682

Courtine, G., Y. Gerasimenko, R. van den Brand, A. Yew, P. Musienko, H. Zhong, B. Song, Y. Ao, R.M. Ichiyama, I. Lavrov, et al. 2009. Transformation of nonfunctional spinal circuits into functional states after the loss of brain input. *Nat. Neurosci.* 12:1333–1342. https://doi.org/10.1038/nn.2401

Flavell, S.W., and M.E. Greenberg. 2008. Signaling mechanisms linking neuronal activity to gene expression and plasticity of the nervous system. *Annu. Rev. Neurosci.* 31:563–590. https://doi.org/10.1146/annurev.neuro.31.060407.125631

Hamers, F.P.T., G.C. Koopmans, and E.A.J. Joosten. 2006. CatWalk-assisted gait analysis in the assessment of spinal cord injury. *J. Neurotrauma.* 23: 537–548. https://doi.org/10.1089/neu.2006.23.537

Hilton, B.J., E. Anenberg, T.C. Harrison, J.D. Boyd, T.H. Murphy, and W. Tetzlaff. 2016. Re-establishment of cortical motor output maps and spontaneous functional recovery via spared dorsolaterally projecting corticospinal neurons after dorsal column spinal cord injury in adult mice. *J. Neurosci.* 36:4080–4092. https://doi.org/10.1523/JNEUROSCI.3386-15.2016

Hollis, E.R. II, N. Ishiko, M. Pessian, K. Tolentino, C.A. Lee-Kubli, N.A. Calcutt, and Y. Zou. 2015. Remodelling of spared proprioceptive circuit involving a small number of neurons supports functional recovery. *Nat. Commun.* 6:6079. https://doi.org/10.1038/ncomms7079

Iwasato, T., A. Datwani, A.M. Wolf, H. Nishiyama, Y. Taguchi, S. Tonegawa, T. Knöpfel, R.S. Erzurumlu, and S. Itohara. 2000. Cortex-restricted disruption of NMDAR1 impairs neuronal patterns in the barrel cortex. *Nature.* 406:726–731. https://doi.org/10.1038/35021059

Jacobi, A., K. Loy, A.M. Schmalz, M. Hellsten, H. Umemori, M. Kerschensteiner, and F.M. Bareyre. 2015. FGF22 signaling regulates synapse formation during post-injury remodeling of the spinal cord. *EMBO J.* 34: 1231–1243. https://doi.org/10.15252/embj.201490578

Jankowska, E., A. Lundberg, W.J. Roberts, and D. Stuart. 1974. A long propriospinal system with direct effect on motoneurones and on interneurones in the cat lumbosacral cord. *Exp. Brain Res.* 21:169–194. https://doi.org/10.1007/BF00234388

Kakizawa, S., M. Yamasaki, M. Watanabe, and M. Kano. 2000. Critical period for activity-dependent synapse elimination in developing cerebellum. *J. Neurosci.* 20:4954–4961. https://doi.org/10.1523/JNEUROSCI.20-13-04954.2000

Katz, L.C., and C.J. Shatz. 1996. Synaptic activity and the construction of cortical circuits. *Science.* 274:1133–1138. https://doi.org/10.1126/science.274.5290.1133

Kerschensteiner, M., F.M. Bareyre, B.S. Buddeberg, D. Merkler, C. Stadelmann, W. Brück, T. Misgeld, and M.E. Schwab. 2004. Remodeling of axonal connections contributes to recovery in an animal model of multiple sclerosis. *J. Exp. Med.* 200:1027–1038. https://doi.org/10.1084/jem.20040452

Krashes, M.J., S. Koda, C. Ye, S.C. Rogan, A.C. Adams, D.S. Cusher, E. Maratos-Flier, B.L. Roth, and B.B. Lowell. 2011. Rapid, reversible activation of AgRP neurons drives feeding behavior in mice. *J. Clin. Invest.* 121: 1424–1428. https://doi.org/10.1172/JCI46229

Lang, C., P.M. Bradley, A. Jacobi, M. Kerschensteiner, and F.M. Bareyre. 2013. STAT3 promotes corticospinal remodelling and functional recovery after spinal cord injury. *EMBO Rep.* 14:931–937. https://doi.org/10.1038/embor.2013.117

Mahler, S.V., and G. Aston-Jones. 2018. CNO Evil? Considerations for the use of DREADDs in behavioral neuroscience. *Neuropsychopharmacology.* 43: 934–936. https://doi.org/10.1038/npp.2017.299

Metsalu, T., and J. Vilo. 2015. ClustVis: a web tool for visualizing clustering of multivariate data using Principal Component Analysis and heatmap. *Nucleic Acids Res.* 43(W1):W566-70. https://doi.org/10.1093/nar/gkv468

Miao, C., Q. Cao, H.T. Ito, H. Yamahachi, M.P. Witter, M.-B. Moser, and E.I. Moser. 2015. Hippocampal remapping after partial inactivation of the medial entorhinal cortex. *Neuron.* 88:590–603. https://doi.org/10.1016/j.neuron.2015.09.051

Okawa, H., M. Hoon, T. Yoshimatsu, L. Della Santina, and R.O.L. Wong. 2014. Illuminating the multifaceted roles of neurotransmission in shaping neuronal circuitry. *Neuron.* 83:1303–1318. https://doi.org/10.1016/j.neuron.2014.08.029

Roth, B.L. 2016. DREADDs for Neuroscientists. *Neuron.* 89:683–694. https://doi.org/10.1016/j.neuron.2016.01.040

Sanes, J.R., and J.W. Lichtman. 1999. Development of the vertebrate neuromuscular junction. *Annu. Rev. Neurosci.* 22:389–442. https://doi.org/10.1146/annurev.neuro.22.1.389

Takeoka, A., and S. Arber. 2019. Functional Local Proprioceptive Feedback Circuits Initiate and Maintain Locomotor Recovery after Spinal Cord Injury. *Cell Reports.* 27:71–85.e3. https://doi.org/10.1016/j.celrep.2019.03.010

Takeoka, A., I. Vollenweider, G. Courtine, and S. Arber. 2014. Muscle spindle feedback directs locomotor recovery and circuit reorganization after spinal cord injury. *Cell.* 159:1626–1639. https://doi.org/10.1016/j.cell.2014.11.019

Tao, H.W., and M.M. Poo. 2005. Activity-dependent matching of excitatory and inhibitory inputs during refinement of visual receptive fields. *Neuron.* 45:829–836. https://doi.org/10.1016/j.neuron.2005.01.046

Tsien, J.Z., D.F. Chen, D. Gerber, C. Tom, E.H. Mercer, D.J. Anderson, M. Mayford, E.R. Kandel, and S. Tonegawa. 1996. Subregion- and cell type-restricted gene knockout in mouse brain. *Cell.* 87:1317–1326. https://doi.org/10.1016/S0092-8674(00)81826-7

Ueno, M., Y. Hayano, H. Nakagawa, and T. Yamashita. 2012. Intraspinal rewiring of the corticospinal tract requires target-derived brain-derived neurotrophic factor and compensates lost function after brain injury. *Brain.* 135:1253–1267. https://doi.org/10.1093/brain/aws053

Ultanir, S.K., J.-E. Kim, B.J. Hall, T. Deerinck, M. Ellisman, and A. Ghosh. 2007. Regulation of spine morphology and spine density by NMDA receptor signaling in vivo. *Proc. Natl. Acad. Sci. USA.* 104:19553–19558. https://doi.org/10.1073/pnas.0704031104

van den Brand, R., J. Heutschi, Q. Barraud, J. DiGiovanna, K. Bartholdi, M. Huerlimann, L. Friedli, I. Vollenweider, E.M. Moraud, S. Duis, et al. 2012. Restoring voluntary control of locomotion after paralyzing spinal cord injury. *Science.* 336:1182–1185. https://doi.org/10.1126/science.1217416

Vong, L., C. Ye, Z. Yang, B. Choi, S. Chua Jr., and B.B. Lowell. 2011. Leptin action on GABAergic neurons prevents obesity and reduces inhibitory tone to POMC neurons. *Neuron.* 71:142–154. https://doi.org/10.1016/j.neuron.2011.05.028

Washbourne, P., J.E. Bennett, and A.K. McAllister. 2002. Rapid recruitment of NMDA receptor transport packets to nascent synapses. *Nat. Neurosci.* 5: 751–759. https://doi.org/10.1038/nn883

Watson, C., G. Paxinos, G. Kayalioglu, and C. Heise. 2009. Atlas of the mouse spinal cord. *In The Spinal Cord.* Elsevier, Amsterdam, Netherlands. pp. 308–379. https://doi.org/10.1016/B978-0-12-374247-6.50020-1

Zeilhofer, H.U., B. Studler, D. Arabadzisz, C. Schweizer, S. Ahmadi, B. Layh, M.R. Bösl, and J.M. Fritschy. 2005. Glycinergic neurons expressing enhanced green fluorescent protein in bacterial artificial chromosome transgenic mice. *J. Comp. Neurol.* 482:123–141. https://doi.org/10.1002/cne.20349

Zörner, B., L.C. Bachmann, L. Filli, S. Kapitza, M. Gullo, M. Bolliger, M.L. Starkey, M. Röthlisberger, R.R. Gonzenbach, and M.E. Schwab. 2014. Chasing central nervous system plasticity: the brainstem's contribution to locomotor recovery in rats with spinal cord injury. *Brain.* 137: 1716–1732. https://doi.org/10.1093/brain/awu078